Proceedings of the Combustion Institute 40 (2024) 105297

Contents lists available at ScienceDirect

Proceedings of the Combustion Institute

journal homepage: www.elsevier.com/locate/proci

Carrier-phase DNS study of particle size distribution effects on iron particle ignition in a turbulent mixing layer

T.D. Luu [a,*], A. Shamooni [b], A. Kronenburg [b], D. Braig [c], J. Mich [c], B.-D. Nguyen [c], A. Scholtissek [c], C. Hasse [c], G. Thäter [d], M. Carbone [e,f], B. Frohnapfel [d], O.T. Stein [a]

[a] Engler-Bunte-Institut, Simulation of Reacting Thermo-Fluid Systems, Karlsruhe Institute for Technology, Engler-Bunte-Ring 7, 76131 Karlsruhe, Germany
[b] Institute for Combustion Technology, University of Stuttgart, Pfaffenwaldring 31, 70569 Stuttgart, Germany
[c] Simulation of Reactive Thermo-Fluid Systems, Technical University of Darmstadt, Otto-Berndt-Straße 2, 64287 Darmstadt, Germany
[d] Institute of Fluid Mechanics, Karlsruhe Institute of Technology, Kaiserstraße 10, 76131 Karlsruhe, Germany
[e] Theoretical Physics I, University of Bayreuth, Universitätsstraße 30, 95447 Bayreuth, Germany
[f] Max Planck Institute for Dynamics and Self-Organisation, Am Faßberg 17, 37077 Göttingen, Germany

ARTICLE INFO

Keywords:
Iron combustion
Metal fuel
Turbulent mixing layer
CP-DNS
Solid fuel combustion
Particle size distribution

ABSTRACT

The ignition and combustion of iron particles in a turbulent mixing layer is studied by means of three-dimensional carrier-phase direct numerical simulations (CP-DNS). A particular focus is set on particle size distribution (PSD) effects on the ignition behaviour by comparing CP-DNS results from using a realistic experimental PSD to DNS data based on a monodisperse (MD) particle cloud with the same equivalence ratio. The CP-DNS solves the Eulerian transport equations of the reacting gas phase and resolves all turbulent scales, while the particle boundary layers are modelled in the Lagrangian point-particle framework. A previously validated sub-model for the oxidation of iron to Wüstite (FeO) that accounts for both diffusion- and kinetically-limited combustion is employed. The mixing layer is initialised with an upper stream of air carrying cold iron particles and an opposed lower stream of hot air. Simulation results show distinct differences in the ignition behaviour between the MD and PSD cases. The ignition of the PSD case is delayed compared to the MD case and does not show any significant particle clustering prior to ignition. Further investigations indicate that the particle size has a crucial effect on the mixing process and ignition time. Small particles start their oxidation process early and already consume some of the available oxygen, while not crucially affecting the gas temperature due to their limited iron mass contribution. Conversely, a slower entrainment into the lower stream combined with higher thermal inertia and the prior oxygen depletion by the small particles leads to a delayed oxidation of the larger particles. As a net result, the PSD case shows a wide spread of individual particle ignition delay times and overall delayed bulk ignition compared to the MD case, where the majority of the particles ignites over a shorter period of time.

1. Introduction

In the next few decades, the global energy demand is expected to rise due to the global industrial growth and increasing world population. Fossil fuels still dominate the energy supply, but their non-renewable nature and negative environmental effects raise the need for alternative sources. Wind and solar energy are renewable and carbon-free, but their limited geographical distribution and high volatility make it difficult to supply regions with high energy demand continuously. A possible solution is the development of new emission-free energy storage technologies. A promising approach is the metal oxidation/reduction cycle based on iron [1,2]. The potential of iron as a carbon-free energy carrier is due to its high energy density and abundance combined with its excellent transport and storage properties [3]. When suitably combining iron oxidation and oxide reduction a sustainable circular zero-carbon energy economy can be achieved [1]. The most significant difference between iron oxidation and classical solid fuel conversion (e.g. coal) is the non-volatile heterogeneous combustion behaviour of iron [4], such that existing modelling strategies for carbon-based solid fuels cannot be used without modification. The current lack of a deeper understanding and reliable models for the relevant physics drive major research efforts to improve our fundamental knowledge on iron flames.

Goroshin et al. [5] proposed a simple analytical model for the heating, ignition and diffusive burnout of single metal particles. Soo

* Corresponding author.
E-mail address: tien.luu@kit.edu (T.D. Luu).

https://doi.org/10.1016/j.proci.2024.105297
Received 4 December 2023; Accepted 28 May 2024
Available online 24 June 2024

et al. [6] developed a kinetically- and diffusion-limited iron combustion model with the major oxidation step of Fe to FeO that was later extended by Hazenberg and van Oijen [7], Thijs et al. [8] and Mich et al. [9]. In [8], improved heat and mass transfer correlations from fully-resolved particle simulations were derived and in [9] polydispersity effects on Euler–Lagrange simulations were studied. Mi et al. [10] proposed an alternative sub-model that describes the growth of FeO and Fe_3O_4 layers by a parabolic rate law. In the past few years, experimental studies on single iron particles [11–13] and iron particle clouds [14–16] in laminar flows have been conducted. Concurrent numerical modelling research has examined various physical aspects such as discreteness [17–19], flame structure and laminar burning velocities [7,20,21].

The transition from laminar to turbulent iron dust flames introduces further challenges. It is known from previous research on volatile-driven solid fuel combustion that turbulent mixing, homogeneous chemistry and solid fuel kinetics are strongly coupled. However, the corresponding coupling processes for non-volatile iron dust flames will likely be different. To investigate these processes in detail, direct numerical simulations (DNS) are essential. Fully-resolved DNS directly simulates the full turbulence spectrum and resolves all particle boundary layers, but due to its high computational cost, it is restricted to single particles [8] and small particle groups [19]. For particle clouds, the carrier-phase DNS (CP-DNS) approach provides a good balance between accuracy and efficiency. CP-DNS resolves all turbulent scales and the flame front, but uses sub-models for the transfer of momentum, heat and mass across the particle boundary layers. CP-DNS of volatile-driven solid fuel combustion from coal or biomass have been conducted by several researchers [22–25]. A first impression of early-time iron cloud combustion in a double mixing layer examined by CP-DNS has been given by Hemamalini et al. [26]. In our previous work [27] we studied the ignition and combustion of a monodisperse iron particle cloud in a turbulent shear layer by means of CP-DNS using the (FOSK) iron sub-model proposed by Mich et al. [9]. Here, we extend our previous work by considering a realistic particle size distribution (PSD) to re-examine the underlying ignition mechanism. The objectives of this paper are to

- examine iron particle cloud ignition in shear-driven turbulence using an experimentally determined PSD,
- characterise the differences between the ignition of simplified monodisperse particle clouds and clouds with a realistic PSD.

2. Modelling approach

2.1. Gas phase

The gas phase is governed by the conservation equations for mass, momentum, enthalpy and chemical species. The Le = 1 assumption is invoked and the mass/heat diffusivities are obtained from Sc = Pr = 0.7. Radiative heat transfer is described by the discrete ordinates method (DOM). Isotropic particle scattering is considered, while the pure air carrier gas does not absorb or emit radiation ($\varepsilon_{\text{gas}} \approx 0.001$). Strictly assuming non-volatile iron conversion, the oxides formed by combustion remain on the particles and homogeneous chemistry is ignored. Gas–solid coupling is achieved via interphase source terms

$$\dot{S}_{\rho,p} = \dot{S}_{\mathrm{O}_2,p} = -\frac{1}{\Delta^3}\sum_{p=1}^{N_p}\frac{dm_p}{dt}, \tag{1}$$

$$\dot{S}_{u,p} = -\frac{1}{\Delta^3}\sum_{p=1}^{N_p}\frac{d(m_p\mathbf{u}_p)}{dt}, \tag{2}$$

$$\dot{S}_{h_s,p} = -\frac{1}{\Delta^3}\sum_{p=1}^{N_p}\left(\frac{m_p c_{\mathrm{p},p}}{\tau_{con}}(T_g - T_p) + \frac{dm_p}{dt}h_{s,\mathrm{O}_2}|_{T_p}\right)$$

with the particle mass m_p, particle (gas) temperature T_p (T_g), convective heat transfer time scale τ_{con}, particle specific heat capacity $c_{\mathrm{p},p}$, sensible enthalpy of consumed oxygen during oxidation at particle temperature $h_{s,\mathrm{O}_2}|_{T_p}$, and the number of particles per cell N_p with edge length Δ.

2.2. Solid phase

The Lagrangian particles are initialised as pure iron. During the oxidation FeO is produced via $\mathrm{Fe}+0.5\mathrm{O}_2 \rightarrow \mathrm{FeO}$ and the thermophysical properties (ρ, c_p and h_s) of Fe and FeO are required. The densities are calculated analogously to [9] and the further thermophysical properties are retrieved from [28] using the Shomate equations. The particle specific heats are obtained from $c_{\mathrm{p},p} = Y_{\mathrm{Fe}}c_{\mathrm{p,Fe}} + Y_{\mathrm{FeO}}c_{\mathrm{p,FeO}}$, with melting and solidification modelled by the apparent heat capacity method [29]. The iron mass conversion rate is determined from the FOSK model by Mich et al. [9]

$$\frac{dm_{p,\mathrm{Fe}}}{dt} = -\frac{1}{s}\rho_f Y_{\mathrm{O}_2} A_d k_d \mathrm{Da}^*, \tag{3}$$

$$\frac{dm_{p,\mathrm{FeO}}}{dt} = \frac{1+s}{s}\rho_f Y_{\mathrm{O}_2} A_d k_d \mathrm{Da}^*, \tag{4}$$

where,

$$\mathrm{Da}^* = \frac{A_r k_r}{A_r k_r + A_d k_d} \tag{5}$$

is the normalised Damköhler number, $A_r = A_d = \pi d_p^2$ the reactive and diffusive areas of the particle (assumed identical), $k_r = k_\infty \mathrm{e}^{-E_a/R_u T_p}$ the rate of kinetic surface reactions and $k_d = \mathrm{Sh}\frac{D_{\mathrm{O}_2,f}}{d_p}$ the diffusive transfer rate. $\mathrm{Sh} = 2 + 0.552\mathrm{Re}_p^{1/2}\mathrm{Sc}^{1/3}$ is the Sherwood number, $\mathrm{Re}_p = \rho_f|\mathbf{u}_g - \mathbf{u}_p|\frac{d_p}{\mu_f}$ the particle Reynolds number and s the mass stoichiometric ratio of the oxidation to iron oxide. Subscript $< f >$ refers to properties at film temperature. Further model coefficients are based on [9], with corresponding model details reported therein.

Only drag force is assumed to act on the particles. Given that the Biot number $\mathrm{Bi} \approx 0.001 - 0.01$ [10], uniform particle temperatures are assumed and governed by convective heat exchange, radiation, heat of combustion and oxygen consumption from the gas phase. Hence, the solid phase governing equations are

$$\frac{dm_p}{dt} = \frac{dm_{p,\mathrm{Fe}}}{dt} + \frac{dm_{p,\mathrm{FeO}}}{dt}, \tag{6}$$

$$\frac{d\mathbf{u}_p}{dt} = \frac{\mathbf{u}_g - \mathbf{u}_p}{\tau_p}, \tag{7}$$

$$\frac{dT_p}{dt} = \frac{1}{\tau_{con}}(T_g - T_p) + \frac{\varepsilon_p A_p \sigma}{m_p c_{p,p}}(\Theta_r^4 - T_p^4) + \frac{\dot{Q}_{\mathrm{FeO}}}{m_p c_{p,p}} + \frac{\dot{Q}_{\mathrm{O}_2}}{m_p c_{p,p}}$$

with the gas velocity at particle position $\mathbf{u}_g$, the particle velocity $\mathbf{u}_p$ and the particle relaxation time $\tau_p = \frac{\rho_p d_p^2}{18\mu_f}(1+0.15\mathrm{Re}_p^{2/3})^{-1}$. $A_p = \frac{1}{4}\pi d_p^2$ is the projected area of the particle, $\varepsilon_p = 0.9$ [30] the particle emissivity, σ the Stefan–Boltzmann constant, Θ_r the gas phase radiation temperature from DOM, $\dot{Q}_{\mathrm{FeO}} = \frac{dm_{p,\mathrm{FeO}}}{dt}\Delta h_{c,\mathrm{FeO}}$ the heat released by Fe oxidation, $\Delta h_{c,\mathrm{FeO}}$ the formation enthalpy of FeO, and $\dot{Q}_{\mathrm{O}_2}$ the energy transfer due to oxygen consumption at T_p. Convective heat transfer follows Ranz-Marshall [31]

$$\tau_{con} = \frac{1}{6}\frac{\mathrm{Pr}}{\mathrm{Nu}}\frac{c_{\mathrm{p},p}}{c_{\mathrm{p},f}}\frac{\rho_p d_p^2}{\mu_f} \tag{8}$$

with $\mathrm{Nu} = 2+0.552\mathrm{Re}_p^{1/2}\mathrm{Pr}^{1/3}$. Sherwood and Nusselt numbers corrected for Stefan flow [32] are considered

$$\mathrm{Sh}^* = \mathrm{Sh}\frac{\ln(1+B_M)}{B_M}, \quad \mathrm{Nu}^* = \mathrm{Nu}\frac{\ln(1+B_T)}{B_T} \tag{9}$$

such that Sh^* and Nu^* replace Sh and Nu in the previous equations. B_M is calculated as

$$B_M = \frac{Y_{\mathrm{O}_2,g} - Y_{\mathrm{O}_2,p}}{Y_{\mathrm{O}_2,p} - 1}, \tag{10}$$

$$Y_{\mathrm{O}_2,p} = Y_{\mathrm{O}_2,g}\frac{A_d k_d}{A_r k_r + A_d k_d} \tag{11}$$

and B_T via

$$B_T = (1 + B_M)^{\varphi}, \quad \varphi = \frac{c_{\mathrm{p,O_2}}|_{T_p}}{c_{\mathrm{p},g}} \frac{\mathrm{Pr}}{\mathrm{Sc}} \tag{12}$$

where $c_{\mathrm{p,O_2}}|_{T_p}$ is the specific heat of oxygen at particle temperature and $c_{\mathrm{p},g}$ the gas specific heat. The iron sub-model considers melting and solidification of Fe and FeO. Therefore, the peak temperature can be higher than the melting point of Fe and FeO, but is typically far below boiling point. Under these conditions the vapour pressure of iron is low and the non-volatile assumption for iron particle combustion remains valid. This also implies negligible nanoparticle formation and deposition effects which do not affect the PSD. As a result of considering melting and solidification, the different densities of Fe (solid or liquid) and FeO (solid or liquid) are all considered in the model, in proportion to the instantaneous mass fractions of Fe and FeO within the particle [9]. Accordingly, the instantaneous properties of each particle reflect the relative contributions of Fe and FeO and their effect on the PSD. The present sub-model for iron particle oxidation has been validated against laser-heated particle combustion experiments published in [11,29] and predictions from [9] in our previous work [27].

3. Computational configuration

A turbulent reacting mixing layer similar to Rieth et al. [23], but based on the evolution of the momentum thickness δ_θ to determine the self-similar regime of the shear-induced turbulence [33] is studied. The upper stream (US) of mixing layer is initialised as air at $T = 550\,\mathrm{K}$ carrying iron particles, while the lower stream (LS) is hot air at $T = 1650\,\mathrm{K}$. The velocity of the two streams is equal but they flow in the opposite x-direction with $\Delta u_x = 30\,\mathrm{m/s}$, see Fig. 1. A hyperbolic tangent profile is used to initialise u_x

$$u_x = \frac{\Delta u_x}{2} \tanh\left(\frac{y - L_y/2}{2\delta_{\theta,0}}\right), \tag{13}$$

with the initial momentum thickness $\delta_{\theta,0}$ corresponding to Reynolds number

$$\mathrm{Re}_{\theta,0} = \frac{\Delta u_x \delta_{\theta,0}}{(\nu_{\mathrm{US}} + \nu_{\mathrm{LS}})/2} = 44.018 \tag{14}$$

with ν_{US} (ν_{LS}) the initial viscosities of the upper (lower) stream. The computational domain has dimensions $L_x = 320 \times \delta_{\theta,0}$, $L_y = 240 \times \delta_{\theta,0}$ and $L_z = 80 \times \delta_{\theta,0}$ and consists of a total of 85M cubic cells with a constant size of $\Delta = 100\,\mu\mathrm{m}$. Spherical iron particles are initialised with the velocity and temperature of their carrying (upper) stream and their number is chosen to initially have $\phi = 1$ in this stream. To evaluate the effect of the PSD on particle ignition, DNS data from the previously studied monodispersed case with a uniform initial $d_p = 10\,\mu\mathrm{m}$ [27] is compared to the present case with 2,175,000 particles initialised with the experimental PSD of Fedoryk et al. [16] ($5\,\mu\mathrm{m} < d_p < 35\,\mu\mathrm{m}$). The size of every Lagrangian particle is tracked individually and dynamically adapts to the considered physics, e.g. increasing particle size due to oxide deposition. To speed up the computations, isotropic velocity perturbations $u'u' = v'v' = w'w' = 0.01\,(\Delta u_x)^2$ with a size of $0.01 \cdot L_x$ generated according to Klein and Kempf et al. [34,35] are initially superimposed on the bulk velocity in the main shear region. The pressure and momentum boundary conditions are periodic in x- and z-direction, while a zero-gradient momentum boundary and ambient pressure is assumed in y-direction.

Following [23], the Kolmogorov length scale is estimated by computing spatial averages $\langle . \rangle$ across the homogeneous x/z-directions. Then, local velocity fluctuations can be calculated as $\mathbf{u}' = \mathbf{u} - \langle \mathbf{u} \rangle$ and the average dissipation becomes $\langle \epsilon \rangle = \langle \tau_{ij} \frac{\partial u_i'}{\partial x_j} \rangle$, with the viscous stress tensor τ_{ij}. Finally, the Kolmogorov length scale is estimated as $\langle \eta \rangle = \left(\frac{\langle \nu \rangle^3}{\langle \epsilon \rangle} \right)^{1/4}$. Following [33], Fig. 2 shows the time evolution of the momentum thickness δ_θ in the present mixing layer, which grows in time with changing slopes that delineate three distinct regions [27].

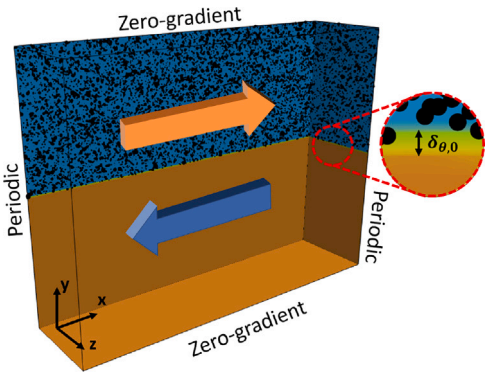

Fig. 1. Initial and boundary conditions of the mixing layer.

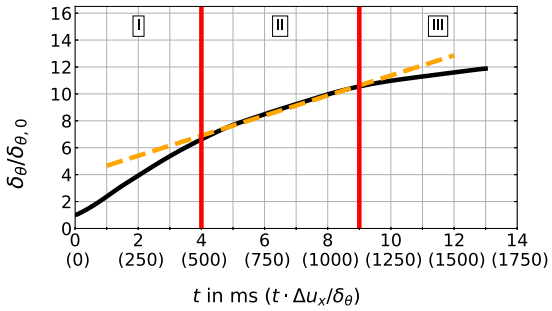

Fig. 2. Time evolution of momentum thickness δ_θ. Vertical red lines delineate the period of self-similarity. (For interpretation of the references to colour in this figure legend, the reader is referred to the web version of this article.)

While region I (initialisation period) and III (boundary effects) are of little interest here, the quasi-linear growth of δ_θ in region II implies a time period of self-similar turbulence for $4 < t < 9\,\mathrm{ms}$. A minimum Kolmogorov length scale of $123\,\mu\mathrm{m}$ is estimated for region II. For a valid CP-DNS, the ideal grid size Δ_{ideal} should follow $d_p \ll \Delta_{ideal} < 2.1\eta$ [36] during the evaluation period, such that all turbulent scales are resolved, while the particles can still be considered as Lagrangian point-particles. With $d_{p,\mathrm{mean}} = 12.7\,\mu\mathrm{m}$, $d_{p,\mathrm{max}} = 35\,\mu\mathrm{m}$, $\Delta = 100\,\mu\mathrm{m}$ and $\eta_{min} = 123\,\mu\mathrm{m}$ the present configuration achieves a reasonable trade-off between all relevant scales.

The simulations are conducted with a low-Mach second order finite volume multiphase solver based on OpenFOAM that has previously been employed for detailed CP-DNS analyses of volatile-driven solid fuel combustion [24,37,38]. A typical CP-DNS simulation costs ≈ 360,000 CPUh on 8192 × AMD-7742 cores.

4. Results and discussion

Fig. 3 gives a visual impression of the temporal evolution of the mixing layer. It shows the gas temperature and particle ensemble in the x-y plane at $L_z/2$, comparing the monodisperse (MD) particle cloud with $d_p = 10\,\mu\mathrm{m}$ from [27] to the present CP-DNS data based on the experimental PSD from [16] with $d_{p,\mathrm{mean}} = 12.7\,\mu\mathrm{m}$ (bottom row). The particles are coloured by their oxidation progress defined as the extent of Fe consumption $C_{\mathrm{ox}} = \frac{m_{\mathrm{Fe},0} - m_{\mathrm{Fe}}}{m_{\mathrm{Fe},0}}$ with $m_{\mathrm{Fe},0}$ and m_{Fe} denoting the initial and instantaneous iron mass inside the particle.

After $t = 4\,\mathrm{ms}$ the initially separated streams (Fig. 1) have developed into a turbulent mixing layer, which leads to the entrainment of cold particles from the upper stream into the hot lower stream, where they heat up and begin their oxidation to FeO, see Fig. 3 (left). A noteable difference between the MD and PSD cases can be observed, where the MD case already shows regions with significantly elevated gas temperatures indicating heat transfer from ignited particles to the gas

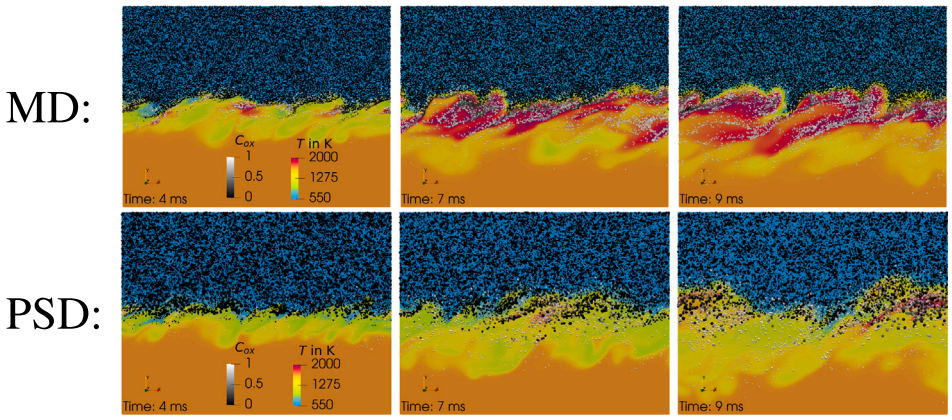

Fig. 3. Time evolution of gas temperature and particles coloured by their oxidation progress C_{ox} in the x-y plane at $L_z/2$. Top: Monodisperse (MD) particle cloud with $d_p = 10\,\mu m$ [27]. Bottom: Particle size distribution (PSD) from experiments [16]. For the PSD case particles are sized proportionally to their instantaneous diameter (but not to scale). (For interpretation of the references to colour in this figure legend, the reader is referred to the web version of this article.)

at $t = 4$ ms, whereas no such increase of T_g can be seen for the PSD case. Both cases already feature partially- (grey) and fully-oxidised (white) particles at this stage, however, the number of fully-oxidised particles is higher for the MD case.

At $t = 7$ ms the MD case shows a large number of particles with significant oxidation progress in the lower stream, which has led to the formation of a continuous flame region (red). This flame region is associated with particle streaks that imply considerable particle clustering. However, there are also clusters with black-coloured particles indicating that at this stage some particles are hampered from their further oxidation by a localised lack of – previously consumed – oxygen (not shown for brevity). In contrast, the PSD case at $t = 7$ ms shows only a small number of fully-oxidised (white) particles and considerably less regions of elevated gas temperatures compared to MD. In these regions, predominantly small particles have $C_{ox} = 1$ (white), while larger particles show less oxidation progress (black...grey). The PSD case also features localised areas of elevated particle number densities, but no strong clustering effects as for the MD case can be observed. At $t = 9$ ms, the continuous flame region of the MD case has grown further and is constantly fed by fresh particles from the upper stream, while the majority of particles in the lower stream is now fully oxidised. The PSD case shows that the local regions of elevated gas temperature have grown and more particles feature $C_{ox} = 1$, but at this stage there is no continuous flame region comparable to the MD case. Summarising Fig. 3, there are strong differences in the ignition behaviour between the MD and the PSD case, with the MD case showing considerable particle clustering and earlier ignition, while particles are more uniformly distributed and ignition occurs later for the PSD case. These findings are corroborated by Fig. 4, which shows the spatially-averaged gas temperature (top) and O_2 mass fraction (bottom) vs. the normalised y-coordinate as a function of time. Comparing the MD (dashed lines) and PSD (continuous lines) cases, it is observed that at $t = 4$ ms (blue) the spatial average of gas temperature shows a localised peak at $y/L_y = 0.5$ for MD, while the corresponding PSD curve has no such peak, implying mostly non-reactive mixing between the two streams. At $t = 7$ ms (green) a local peak also appears for the PSD case, however, the corresponding MD peak is already much higher and even exceeds the lower stream temperature (1650K). The spatially-averaged profiles of Y_{O_2} in Fig. 4 (bottom) characterise the mean O_2 consumption and confirm the previous impression of earlier ignition and combustion for the MD case, as the MD profiles always indicate more O_2 depletion than for the PSD case at corresponding times.

Fig. 5 shows number- and mass-based averages of particle oxidation progress vs. time, where only particles that have at least 5% oxidation progress are considered, to exclude the majority of fully unreacted particles far in the upper stream at early times, see e.g. Fig. 3 at $t = 4$ ms. It

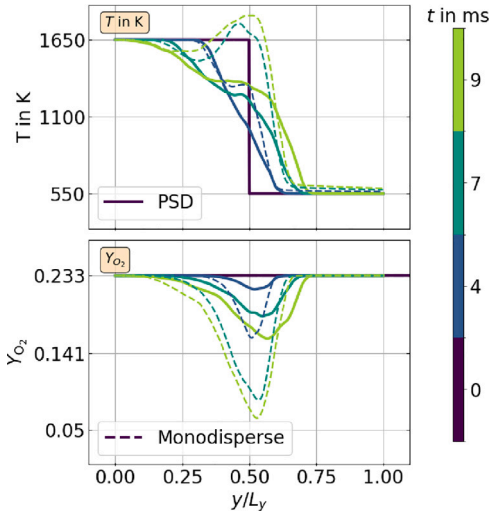

Fig. 4. Spatially-averaged gas temperature (top) and O_2 mass fraction (bottom) as a function of y/L_y and time. MD (dashed lines) and PSD (continuous lines). (For interpretation of the references to colour in this figure legend, the reader is referred to the web version of this article.)

Table 1
Definition of the particle size classes.

Name	Definition in μm
Class1	$5 < d_p \leq 10$
Class2	$10 < d_p \leq 15$
Class3	$15 < d_p \leq 35$

can be seen that the number-based average oxidation progress (black) of the PSD case is always higher than for MD, implying that at any given time a larger fraction of particles has ignited when considering the PSD. This initially also holds for the mass-averages (blue), but this trend is inverted at $t = 5$ ms, when the mass-averaged C_{ox} of the MD case exceeds the one of the PSD case. However, irrespective of the averaging method, at early times the PSD case shows a larger average particle oxidation state than the MD case, which seems in apparent contrast to the earlier ignition for MD found in Figs. 3 and 4. To further investigate the ignition behaviour of typical particle sizes, the particle ensemble of the PSD case is subdivided into a set of particle size classes for data analysis. Different variants of particle size classes have been applied in post-processing, but only a limited influence of these variants has been found. As a result, the particles are grouped in accordance with their most characteristic trends, where every particle is allowed to

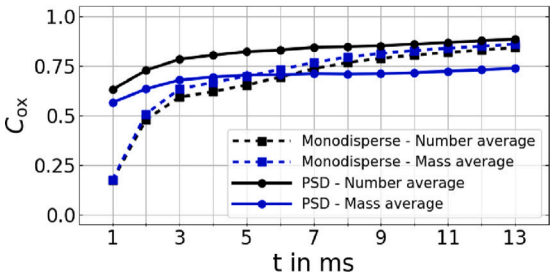

Fig. 5. Number- and mass-based average of oxidation progress C_{ox} vs. time (particles with $C_{ox} > 0.05$ only). (For interpretation of the references to colour in this figure legend, the reader is referred to the web version of this article.)

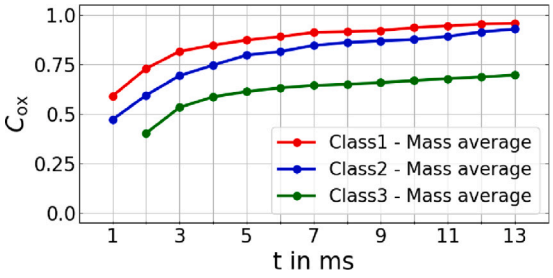

Fig. 6. Mass-averaged oxidation progress for different size classes of the PSD case (particles with $C_{ox} > 0.05$ only). (For interpretation of the references to colour in this figure legend, the reader is referred to the web version of this article.)

adhere to the physics related to its individual temporal evolution and all particles follow the same assumptions. The final sub-division splits the entire particle ensemble into three particle size classes, according to Table 1 and the (mass-)averaged oxidation progress of each class is shown in Fig. 6. It can be seen that the high average particle conversion progress of the PSD case at early times in Fig. 5 is attributed to the small particle sizes only. In particular, the smallest size *Class1* is subject to the combined effect of strong entrainment into the lower stream (lowest Stokes number) and comparatively fast heat-up (largest surface-area-to-volume ratio for small particles) leading to a faster oxidation process, whereas larger particles have a slow entrainment and heat-up, and therefore lower average C_{ox} throughout the simulation. However, despite the earlier conversion of the smallest particles for the PSD case, the mass of iron fuel m_{Fe} and associated heat release is rather limited for *Class1*, such that their impact on the gas temperature remains low. Moreover, the larger surface-to-volume ratio and ability to follow turbulent fluctuations promptly also leads to a faster dissipation of the heat released by the oxidation of the small particles. In contrast, the larger particles require significantly more time to heat up and ignite, such that their slow conversion and delayed heat release postpones bulk ignition. As a net consequence, the uniform particle size of the MD case leads to a more simultaneous heat-up, ignition and solid-to-gas heat transfer, and therefore earlier bulk ignition compared to the investigated PSD case. The latter case shows earlier ignition of individual small particles with little specific heat release, but a much delayed conversion of the larger particles and therefore a globally delayed bulk ignition, as found in Figs. 3 and 4.

Fig. 7 shows scatterplots of particle oxidation progress C_{ox} vs. the normalised y/L_y coordinate for particles in the PSD with $C_{ox} > 0.05$ at different times. Particles are coloured by their surrounding gas oxygen mass fraction Y_{O_2}. It is observed that the smallest *Class1* particles undergo oxidation without any major limitations due the initial abundance of available oxygen (mostly red...yellow scatter), whereas the largest *Class3* particles see increasingly lacking oxygen at late simulation times. This is particularly true for the central region of the mixing layer where the smallest particles lead to early oxygen depletion, while all particle sizes can still find enough oxygen when

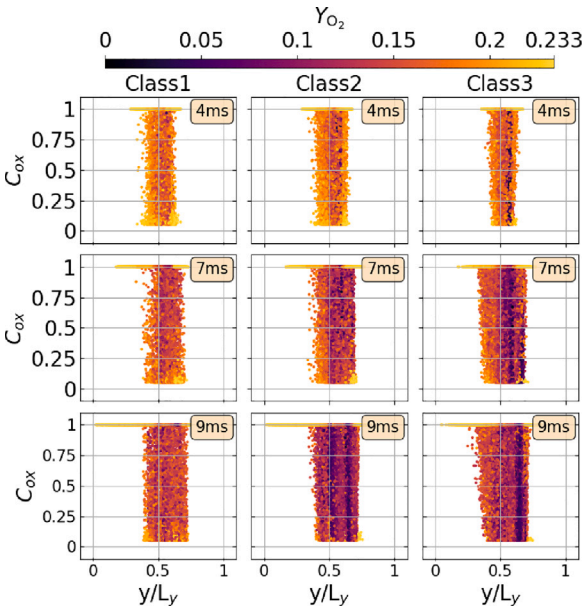

Fig. 7. PSD case, scatterplot of C_{ox} vs. y/L_y coloured by the gas oxygen mass fraction Y_{O_2} surrounding the particles at different times (particles with $C_{ox} > 0.05$ only). (For interpretation of the references to colour in this figure legend, the reader is referred to the web version of this article.)

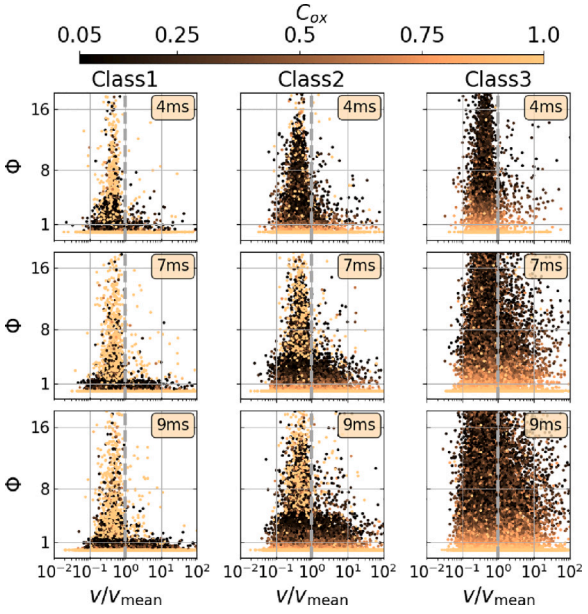

Fig. 8. PSD case, scatterplot of the equivalence ratio surrounding the particles Φ vs. normalised Voronoi volume v/v_{mean} at different times (particles with $C_{ox} > 0.05$ only). (For interpretation of the references to colour in this figure legend, the reader is referred to the web version of this article.)

entrained into the upper and particularly the far lower stream (yellow particles for $y/L_y \to 0$).

Fig. 8 shows scatterplots of the (oxygen-based) equivalence ratio Φ [9] vs. normalised Voronoi volume coloured by particle oxidation progress C_{ox} for the PSD case. The Voronoi volume is a commonly used indicator for particle clustering, with small Voronoi volumes indicating small particle distances, i.e. strong particle clustering. Voronoi volumes of all particles are computed [39] and normalised by the mean Voronoi volume in the entire domain. At all times shown in Fig. 8, all particle size classes exhibit a fraction of particles with $\Phi \to 0$ and $C_{ox} \to 1$, i.e. fully oxidised particles in a very lean oxygen environment. This would not occur in gas combustion, where very lean mixtures cannot

ignite, while heterogeneous iron combustion allows for locally stoichiometric conditions (prior to the shown state of these particles) that lead to full particle conversion. Comparing the oxidation state (particle colour) and equivalence ratio (ordinate) for various size classes and times in Fig. 8, it is observed that the largest *Class3* particles show increasingly higher C_{ox} with $\Phi \rightarrow 0$, whereas the smallest *Class1* particles do not show a similarly clear trend, with a considerable number of fully oxidised small particles at high equivalence ratios. This is because small particles may have already consumed enough oxygen for full particle conversion, before being entrained into regions with many unreacted (larger) particles such that the local equivalence ratio is very high. In contrast, larger particles contain more mass and therefore contribute more strongly to locally large equivalence ratios, in particular when they form clusters. Since particle conversion of the large particles is generally delayed, Fig. 6, large particles are mostly exposed to rich conditions in regions where small particles have previously consumed O_2, which slows down their oxidation progress even further. As a result, the conversion of large *Class3* particles strongly correlates with decreasing equivalence ratio, indicating a reduced availability of oxygen. Considering the normalised Voronoi volume as an indicator for particle clustering, it can be seen that small *Class1* particles tend to have smaller than average Voronoi volumes, whereas the largest *Class3* particles show a wide distribution of Voronoi volumes around the mean. Overall, only a weak dependence of the particle oxidation progress on particle clustering can be observed in Fig. 8, in line with the qualitatively weaker clustering behaviour of the PSD case already seen in Fig. 3.

5. Conclusion

The ignition and combustion of iron particles in a turbulent mixing layer is studied by means of CP-DNS and the results from a monodispersed particle cloud are compared to equivalent data that assumes an experimental PSD [16]. The MD and PSD cases show different bulk ignition characteristics, which is attributed to the different behaviour of individual particle sizes for the PSD case. While small particles are quickly entrained into the lower stream, where they ignite early and partially consume the available oxygen, large particles ignite significantly later due delayed entrainment, higher thermal inertia, and previous oxygen depletion by the small particles. As a net effect, bulk ignition in the MD case occurs more uniformly and globally earlier, whereas the wide distribution of individual particle ignition times leads to later global ignition for the PSD. The PSD case shows less clustering effects compared to the MD case and only a weak effect of clustering on ignition.

The present work extends our previous CP-DNS study on monodisperse iron particle combustion in shear-driven turbulence [27] to polydisperse conditions based on a realistic experimental PSD. Based on this, a myriad of further physical effects that may affect iron particle cloud ignition and combustion can be explored. Such possibly interesting effects include ballistic particle motion vs. turbophoresis, Stokes number effects on particle spatial distributions and clustering, radiation sub-models, cooling due to thermal inertia, turbulence modulation due to reacting particles, just to name a few. These remaining questions are beyond the scope of the present study, but leave an extremely rich field of exploration for the metal combustion research community in future work.

Novelty and significance statement

- Combustion of metals offers a great opportunity for CO_2-free energy conversion.
- Detailed fundamental analysis of particle size distribution (PSD) effects on the ignition of iron particle clouds in shear-driven turbulence.
- This research reveals clear differences between the ignition behaviour of monodispersed and polydispersed iron particle clouds in turbulence.
- The obtained fundamental knowledge can guide future burner designs for iron particle combustion.

CRediT authorship contribution statement

T.D. Luu: Methodology, Software, Validation, Formal analysis, Investigation, Data curation, Visualisation, Writing – original draft. **A. Shamooni:** Methodology, Software, Validation, Formal analysis, Writing – review & editing. **A. Kronenburg:** Conceptualization, Supervision, Funding acquisition, Writing – review & editing. **D. Braig:** Methodology, Software, Validation, Writing – review & editing. **J. Mich:** Methodology, Software, Validation, Writing – review & editing. **B.-D. Nguyen:** Methodology, Software, Validation, Writing – review & editing. **A. Scholtissek:** Conceptualization, Writing – review & editing. **C. Hasse:** Conceptualization, Supervision, Funding acquisition, Writing – review & editing. **G. Thäter:** Methodology, Software, Validation, Writing – review & editing. **M. Carbone:** Conceptualization, Writing – review & editing. **B. Frohnapfel:** Conceptualization, Supervision, Funding acquisition, Writing – review & editing. **O.T. Stein:** Conceptualization, Resources, Supervision, Project administration, Writing – review & editing, Funding acquisition.

Declaration of competing interest

The authors declare that they have no known competing financial interests or personal relationships that could have appeared to influence the work reported in this paper.

Acknowledgements

This work is conducted within the *Clean Circles* research initiative financially supported by KIT Strategiefonds and the Hessian Ministry of Higher Eduction, Research, Science and the Arts. The authors gratefully acknowledge the financial support by the Helmholtz Association of German Research Centres (HGF), within the research field *Energy*, program *Materials and Technologies for the Energy Transition (MTET)*. We acknowledge support by the state of Baden-Württemberg through bwHPC and are grateful for HPC time on HLRS Hawk.

References

[1] J.M. Bergthorson, Recyclable metal fuels for clean and compact zero-carbon power, Prog. Energy Combust. Sci. 68 (2018) 169–196.
[2] P. Debiagi, R.C. Rocha, A. Scholtissek, J. Janicka, C. Hasse, Iron as a sustainable chemical carrier of renewable energy: Analysis of opportunities and challenges for retrofitting coal-fired power plants, Renew. Sustain. Energy Rev. 165 (2022) 112579.
[3] J.M. Bergthorson, S. Goroshin, M.J. Soo, P. Julien, J. Palecka, D.L. Frost, D.J. Jarvis, Direct combustion of recyclable metal fuels for zero-carbon heat and power, Appl. Energy 160 (2015) 368–382.
[4] S. Goroshin, J. Palečka, J.M. Bergthorson, Some fundamental aspects of laminar flames in nonvolatile solid fuel suspensions, Prog. Energy Combust. Sci. 91 (2022) 100994.
[5] S. Goroshin, M. Bidabadi, J.H.S. Lee, Quenching distance of laminar flame in aluminum dust clouds, Combust. Flame 105 (1996) 147–160.
[6] M. Soo, S. Goroshin, J.M. Bergthorson, D.L. Frost, Reaction of a particle suspension in a rapidly-heated oxidizing gas, Prop. Expl. Pyrotechn. 40 (2015) 604–612.
[7] T. Hazenberg, J.A. van Oijen, Structures and burning velocities of flames in iron aerosols, Proc. Combust. Inst. 38 (2021) 4383–4390.
[8] L.C. Thijs, C.E.A.G. van Gool, W.J.S. Ramaekers, J.G.M. Kuerten, J.A. van Oijen, L.P.H. de Goey, Improvement of heat- and mass transfer modeling for single iron particles combustion using resolved simulations, Combust. Sci. Technol. 1 (2022) 1–17.
[9] J. Mich, D. Braig, T. Gustmann, C. Hasse, A. Scholtissek, A comparison of mechanistic models for the combustion of iron microparticles and their application to polydisperse iron-air suspensions, Combust. Flame 256 (2023) 112949.
[10] X. Mi, A. Fujinawa, J.M. Bergthorson, A quantitative analysis of the ignition characteristics of fine iron particles, Combust. Flame 240 (2022) 112011.
[11] D. Ning, Y. Shoshin, J.A. van Oijen, G. Finotello, L.P.H. de Goey, Burn time and combustion regime of laser-ignited single iron particle, Combust. Flame 230 (2021) 111424.
[12] A. Panahi, D. Chang, M. Schiemann, A. Fujinawa, X. Mi, J.M. Bergthorson, Y.A. Levendis, Combustion behavior of single iron particles-part I: An experimental study in a drop-tube furnace under high heating rates and high temperatures, Appl. Energy Combust. Sci. 13 (2023) 100097.

[13] D. Ning, T. Li, J. Mich, A. Scholtissek, B. Böhm, A. Dreizler, Multi-stage oxidation of iron particles in a flame-generated hot laminar flow, Combust. Flame 256 (2023) 112950.
[14] F.-D. Tang, S. Goroshin, A. Higgins, J. Lee, Flame propagation and quenching in iron dust clouds, Proc. Combust. Inst. 32 (2009) 1905–1912.
[15] M. McRae, P. Julien, S. Salvo, S. Goroshin, D.L. Frost, J.M. Bergthorson, Stabilized, flat iron flames on a hot counterflow burner, Proc. Combust. Inst. 37 (2019) 3185–3191.
[16] M. Fedoryk, B. Stelzner, S. Harth, D. Trimis, Experimental investigation of the laminar burning velocity of iron-air flames in a tube burner, Appl. Energy Combust. Sci. 13 (2023) 100111.
[17] F.-D. Tang, A.J. Higgins, S. Goroshin, Propagation limits and velocity of reaction-diffusion fronts in a system of discrete random sources, Phys. Rev. E 85 (2012) 036311.
[18] F. Lam, X. Mi, A.J. Higgins, Front roughening of flames in discrete media, Phys. Rev. E 96 (2017) 013107.
[19] F.H. Vance, A. Scholtissek, H. Nicolai, C. Hasse, Flame propagation modes for iron particle clusters in air, Part II: Transition from continuous to discrete propagation mode under strong convection effects, Combust. Flame (2023) 113199.
[20] A. Ravi, P. de Goey, J. van Oijen, Flame structure and burning velocity of flames propagating in binary iron aerosols, Proc. Combust. Inst. 39 (2023) 3573–3581.
[21] X. Wen, A. Scholtissek, J. van Oijen, J. Bergthorson, C. Hasse, Numerical modeling of pulverized iron flames in a multidimensional hot counterflow burner, Combust. Flame 248 (2023) 112572.
[22] T. Hara, M. Muto, T. Kitano, R. Kurose, S. Komori, Direct numerical simulation of a pulverized coal jet flame employing a global volatile matter reaction scheme based on detailed reaction mechanism, Combust. Flame 162 (2015) 4391–4407.
[23] M. Rieth, A.M. Kempf, A. Kronenburg, O.T. Stein, Carrier-phase DNS of pulverized coal particle ignition and volatile burning in a turbulent mixing layer, Fuel 212 (2018) 364–374.
[24] A. Shamooni, P. Debiagi, B. Wang, T.D. Luu, O.T. Stein, A. Kronenburg, G. Bagheri, A. Stagni, A. Frassoldati, T. Faravelli, A.M. Kempf, X. Wen, C. Hasse, Carrier-phase DNS of detailed NO_x formation in early-stage pulverized coal combustion with fuel-bound nitrogen, Fuel 291 (2021) 119998.
[25] G. Chen, H. Wang, K. Luo, J. Fan, A DNS study of pulverized coal combustion in a hot turbulent environment: Effects of particle size, mass loading and preferential concentration, Combust. Flame 254 (2023) 112839.
[26] S.S. Hemamalini, S. Guhathakurta, J.A. van Oijen, B. Cuenot, X.C. Mi, On the interaction between burning iron particles and turbulence: A study via mesoscale-resolved simulations, in: Proc. Euro. Combust. Meet., 2023.
[27] T.D. Luu, A. Shamooni, A. Kronenburg, D. Braig, J. Mich, B.-D. Nguyen, A. Scholtissek, C. Hasse, G. Thäter, M. Carbone, B. Frohnapfel, O.T. Stein, Carrier-phase DNS of ignition and combustion of iron particles in a turbulent mixing layer, Flow Turb. Combust. (2024).
[28] M.W. Chase, NIST-JANAF Thermochemical Tables, fourth ed., vol. 9, Am. Inst. Phys., Gaithersburg, 1998.
[29] L.C. Thijs, C.E.A.G. van Gool, W.J.S. Ramaekers, J.A. van Oijen, L.P.H. de Goey, Resolved simulations of single iron particle combustion and the release of nano-particles, Proc. Combust. Inst. 39 (2023) 3551–3559.
[30] G.K. Burgess, P.D. Foote, The Emissivity of Metals and Oxides: IV. Iron Oxide, first ed., vol. 12, U.S. Government Printing Office, Washington, 1916.
[31] W.E. Ranz, J. Marshall, Evaporation from drops - Part 1, Chem. Eng. Progr. 48 (1952) 141–146.
[32] D.B. Spalding, Combustion and Mass Transfer, first ed., Pergamon Press, London, 1979, pp. 51–81.
[33] J. O'Brien, J. Urzay, M. Ihme, P. Moin, A. Saghafian, Subgrid-scale backscatter in reacting and inert supersonic hydrogen-air turbulent mixing layers, J. Fluid Mech. 743 (2014) 554–584.
[34] M. Klein, A. Sadiki, J. Janicka, A digital filter based generation of inflow data for spatially developing direct numerical or large eddy simulations, J. Comput. Phys. 186 (2003) 652–665.
[35] A. Kempf, S. Wysocki, M. Pettit, An efficient, parallel low-storage implementation of Klein's turbulence generator for LES and DNS, Comput. & Fluids 60 (2012) 58–60.
[36] S.B. Pope, Turbulent Flows, Cambridge University Press, Cambridge, 2000.
[37] X. Wen, A. Shamooni, O.T. Stein, L. Cai, A. Kronenburg, H. Pitsch, A.M. Kempf, C. Hasse, Detailed analysis of early-stage NO formation in turbulent pulverized coal combustion with fuel-bound nitrogen, Proc. Combust. Inst. 38 (2020) 4111–4119.
[38] B. Wang, A. Shamooni, O.T. Stein, A. Kronenburg, A.M. Kempf, P. Debiagi, C. Hasse, Investigation of turbulent pulverized solid fuel combustion with detailed homogeneous and heterogeneous kinetics, Energy Fuels 35 (2021) 7077–7091.
[39] C.H. Rycroft, VORO++: A three-dimensional Voronoi cell library in C++, Chaos 19 (2009) 041111.